sensors

MDPI

*Article, Review*

# Small All-range Lidar for Asteroid and Comet Core Missions

**Xiaoli Sun [1,*], Daniel R. Cremons [1], Erwan Mazarico [1], Guangning Yang [1], James B. Abshire [1,2], David E. Smith [3], Maria T. Zuber [3], Mark Storm [4], Nigel Martin [4], Jacob Hwang [4], Jeff D. Beck [5], Nathan R. Huntoon [5], and Dick M. Rawlings [5]**

[1] NASA Goddard Space Flight Center, Greenbelt, Maryland 20771, USA; xiaoli.sun-1@nasa.gov
[2] Department of Astronomy, University of Maryland, College Park, Maryland 20742, USA; james.b.abshire@nasa.gov
[3] Department of Earth, Atmospheric and Planetary Sciences, Massachusetts Institute of Technology, Cambridge, Massachusetts 02139, USA; smithde@mit.edu
[4] Fibertek Inc., Herndon, Virginia 20171, USA; mstorm@fibertek.com
[5] Leonardo DRS Electro-Optical Infrared Systems., Dallas, Texas 75243, USA; jeff.beck@drs.com
* Correspondence: xiaoli.sun-1@nasa.gov; Tel.: +1 301-614-6732

**Abstract:** We report the development of a new class of space lidar specifically designed for planetary small-body missions for both topographic mapping and operational support of sample collection or landing. The instrument is designed to have a wide dynamic range with several operation modes for different mission phases. The laser transmitter consists of a fiber laser that is intensity modulated with a return-to-zero pseudo-noise (RZPN) code. The receiver detects the coded pulse-train and the target range is retrieved by correlating the detected signal with the RZPN kernel. Unlike regular pseudo noise (PN) lidars, the RZPN kernel is set to zero outside laser firing windows, which removes most of the background noise over the receiver integration time. This technique enables the use of low peak-power but high pulse-rate lasers, such as fiber lasers, for long-distance ranging without aliasing. The laser power and the internal gain of the detector can both be adjusted to give a wide system dynamic range. The laser modulation code pattern can also be reconfigured in orbit to best fit to different measurement environments. The receiver uses a multi-pixel linear mode photon-counting HgCdTe APD array with near quantum limited sensitivity at near to mid infrared wavelengths where most of the fiber lasers and diode lasers operate. In addition to range, the lidar can also measure the receive pulse energy and hence the target reflectance to the laser light. The instrument is modular and versatile and can be built mostly with components developed by the optical communication industry.

**Keywords:** lidar; remote sensing; pseudo-noise code

**Citation:** Lastname, F.; Lastname, F.; Last-name, F. Title. *Sensors* **2021**, *21*, x. https://doi.org/10.3390/xxxxx

Received: date
Accepted: date
Published: date

**Publisher's Note:** MDPI stays neutral with regard to jurisdictional claims in published maps and institutional affiliations.

**Copyright:** © 2020 by the authors. Submitted for possible open access publication under the terms and conditions of the Creative Commons Attribution (CC BY) license (http://creativecommons.org/licenses/by/4.0/).

## 1. Introduction

Lidar (light detection and ranging) instruments have been used for planetary remote sensing to measure surface elevation, shape, tidal deformation, spin axis, and reflectance [1-4]. Lidars are also essential tools for studying small planetary bodies, such as asteroids and comet cores, for determining the shape, rotational and orbital dynamics, and surface structure and interior properties along with gravity measurements [5-9]. Asteroids and comet cores are generally much smaller than major planets but they tend to have irregular shapes. Combined with the low-gravity environment, the spacecraft orbit configurations for different science observations often result in a wide range of orbital altitudes above the surface. Therefore, a small-body lidar has to have a wider dynamic than previous planetary lidars that have operated in near-circular mapping orbits. The lidar should also support other mission operations, including reconnaissance from a long distance and landing or sample collection down to near zero distance. Conventional orbiting lidar, such as those described in [3], do not have the necessary operational flexibility and dynamic

range. Here we describe a Small All-range Lidar (SALi) designed specifically for small planetary body missions. It uses a fiber laser with return-to-zero pseudo-noise (RZPN) code laser modulation and correlation detection, and a near quantum limited and pixelated linear mode single photon sensitive detector. They can be built at potentially much lower cost by leveraging on the technology development by the laser communication industry. The combination of these new technologies collectively represents a new class of planetary lidar especially suited for small body missions.

Small planetary bodies are remnants of planetary formation, preserving constituents indicative of conditions in the early Solar System in unique, mostly pristine settings. Numerous astronomical surveys of asteroids [10-12] have taught us about their population, with implications for the dynamical evolution of the solar system [13,14]. The near-Earth object (NEO) population also poses a threat of Earth impact and a better understanding of their internal structure can help in the development of mitigation strategies. Several planetary missions have flown to asteroids and comets for extensive surveys from orbit [15-22]. The lidars on Hayabusa2 and OSIRIS-REx were shown to be essential science instruments for measuring the shape, gravity, and morphology of the asteroids to help us understand their internal structure and their formation. The shape data collected by the lidars were also essential for spacecraft guidance, navigation, and control (GN&C) operation during touch down and sample collection.

For small planetary body investigations, the spacecraft orbital altitude and the ground track speed (cm/s to m/s) are much lower than those of major planets because of the small body size and the low gravity environment. Most of the measurements do not require a high-power laser and large receiver collecting area. The major technical challenge in the lidar design is the flexibility and receiver dynamic range because of the irregular shape of the body and the wide range of orbit altitude. Besides mapping at mid altitude, the lidar is expected to provide a coarse measurement of the shape and rotation axis of the body from a high altitude during the reconnaissance phase of the mission. It is also highly desirable that a single lidar can provide real time spacecraft altitude and velocity data to the spacecraft GN&C system during descent and touchdown. A multi-beam or scanning lidar is preferred to improve the spatial coverage and provide surface slope and roughness measurements.

There have been several asteroid lidars flown over the past 25 years [6-9]. They were similar in design to previous planetary lidars but with lower laser pulse energy and a smaller receiver telescope size. They all use diode pumped Q-switched Nd:YAG lasers which had fixed output pulse energy and limited dynamic range. They were mostly designed for mapping the objects from a nominal orbit altitude. For descent and touchdown, a separate navigation Doppler lidar (NDL) [23,24] is planned for spacecraft altitude and velocity measurements. For safe and precise landing short-range hazard detection lidars (HDL) are also being developed [25]. The Chang'E 4 lunar lander used a flash lidar during the descent starting 100 m above the surface [26]. A flash lidar illuminates an area of the target with a laser pulse and uses a pixelated detector to provide a 3-D image of the target from that single laser pulse. Flash lidars are ideal for hazard avoidance but cannot range over long distances because the laser pulse energy is spread out over the entire scene. The OSIRIS-REx mission carries both a science mapping lidar [9] and a GN&C flash lidar [27]. When a 3-D model of the asteroid is obtained from an orbiting lidar and detailed camera images of the landing area are available, precision touchdown and sample collection can be achieved by tracking surface features without an HDL. A simple laser ranger is still desired to provide the spacecraft range and velocity to the target area.

Our SALi instrument is specially designed for small body missions. It features three new technologies. First, a RZPN code is used to modulate the laser transmitter. The receiver detects the laser pulse pattern instead of individual laser pulses by correlating the received signal with the RZPN kernel [28]. This technique enables the use of low peak-power lasers for long-distance ranging without aliasing. It uses a patented ternary (*i.e.*, -1, 0, 1) RZPN kernel [28], which significantly reduces the effects of background noise and

the detector dark noise compared to conventional pseudo noise (PN) lidar. Second, SALi uses optical fiber lasers developed by the laser communication industry for which the output power can be continuously adjusted over a wide range. Third, it uses a new linear mode photon counting HgCdTe avalanche photodiode (APD) array with near quantum limited sensitivity from visible to mid-infrared wavelength [29], which maximizes the receiver sensitivity and gives long-distance ranging capability. The APD gain can be adjusted from unity to above 1000 with little excess noise and the APD array gives linear analog outputs over a wide dynamic range. SALi is designed to operate in three modes: a coarse survey mode from a long distance, a precision mapping mode from a mid-altitude orbit, and a real-time GN&C sensor mode for touchdown and sample collection. This paper describes the RZPN lidar technique, the SALi instrument design, and the expected performance.

## 2. RZPN Lidar Technique

### *2.1. PN Code Lidars*

The PN code ranging technique has long been used for radio frequency (RF) ranging systems, such as in the Global Positioning System (GPS). PN code lidars have already been used for range measurements [30-33]. A PN code has the advantageous property that it has no apparent correlation with other binary sequences or itself unless it is perfectly aligned in time [34]. In a PN code lidar, the laser is modulated by a binary PN code sequence. The received signal is cross-correlated with a bi-polar form of the code, called the kernel, which is equal to +1 for binary code value "1" and -1 for binary code value "0". The number of binary bits in a PN code sequences is given by $N_b = 2^m - 1$ with $m$ an integer. There are $(N_b + 1)/2$ ones and $(N_b - 1)/2$ zeros in the sequence. The normalized cross correlation of the code and the kernel is equal to unity when the code and kernel line up bit by bit and equal to $2/(N_b + 1)$ everywhere else. The ones and zeros occur at random statistically, thus the term pseudo-noise and the useful correlation properties. Unless the PN code matches the kernel in pattern and time, the kernel effectively randomizes the received signal and background noise by multiplying them by +1 or -1 at random and cancels them out upon correlation. The correlation function peaks when the input signal matches the kernel. The peak value of the correlation function is equal to the total number of received signal photons, which gives the surface reflectance. The peak location in time gives the signal delay or the laser pulse time-of-flight from which the target range can be determined. The ranging precision can be improved by sampling the received signal at a time interval that is a fraction of the laser pulse width [35,36]. The correlator output is periodic and hence there is range ambiguity which is determined by the code length.

PN code lidar enables the use of low-peak power laser transmitters for long distance ranging. The receiver sensitivity increases with the received integration time, which allows a tradeoff between the maximum range and measurement rate. A major shortcoming of a conventional PN code lidar is its susceptibility to background illumination and detector dark noise because of the relatively long receiver integration time.

### *2.2. RZPN Code Lidars*

We have developed a variant of the PN code and kernel, which retains all the advantages of a regular PN lidar but is much less susceptible to background noise [28]. In this approach, the laser is only on at the beginning of the PN code bit interval for a short time and off, hence return-to-zero, for the rest of the bit period. The RZPN kernel takes the same values as the PN code kernel but returns to zero for the reminder of the bit time, as shown in Figure 1. The RZPN lidar technique has been successfully demonstrated in the lab and the field with a breadboard instrument [36,37].

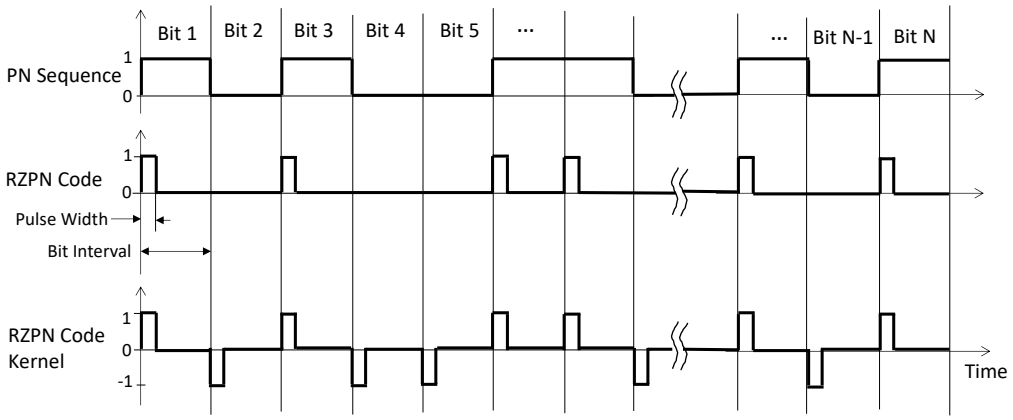


**Figure 1.** Schematic of a binary PN sequence (top), the corresponding RZPN code for the laser modulation (middle), and the kernel to be used for the correlation detection (bottom).

There are three major advantages to the RZPN lidar technique. First, it nulls out all background noise in the return-to-zero time period when calculating the correlation function. Second, it improves the ranging precision with its shorter laser pulse width. Third, it provides space in the remaining bit intervals for additional measurement channels without direct interference as long they use different RZPN codes. The technique provides a new degree of freedom in PN code lidar design, namely, the laser pulse width, provided the average laser output power can stay the same. The higher the laser peak power and the shorter the pulse width are, the better the receiver performance becomes. It is especially suited for fiber lasers where the pulse width and peak power can be continuously varied under the same average power over a wide range.

### *2.3. RZPN Code Detection*

Assuming a rectangular pulse shape, a transmitted laser signal in a RZPN code lidar over one code length period can be expressed as

$$x(t) = E_t \sum_{i=0}^{N_b-1} a_i \, u(t - iT_b), \tag{1}$$

where $E_t$ is the laser pulse energy, $N_b$ is the number of bits in the underlining PN code, $a_i$ is the binary code sequence, equal to 1 or 0, $T_b$ is the bit interval, and $u(t)$, is the unit pulse function given by

$$u(t) = \begin{cases} \frac{1}{T_p}, & 0 \le t \le T_p \\ 0, & else \end{cases} \tag{2}$$

with $T_p$ the laser pulse width. For RZPN code modulation, $T_p < T_b$. The RZPN code period is equal to the number of bits in the code times the bit interval. The laser pulse width, or pulse duty cycle, is a parameter to be optimized.

The received signal is the convolution of the transmitted signal and the target impulse response function, $h_T(t)$, which can be written as

$$y(t) = \int_0^\infty h_T(t - \tau_1) x(\tau_1) d\tau_1. \tag{3}$$

The normalized correlation function of the received signal and the kernel is given by

$$z(t) = \left(\frac{2}{N_b+1}\right) \cdot \left(\frac{T_p}{E_t}\right) \cdot \int_0^{T_s} y(\tau_2) \, k(\tau_2 + t) d\tau_2, \tag{4}$$

where $T_s = N_b T_b$ is the code length time period and $k(t)$ is the RZPN code kernel, which is a periodic function. Over one code length period the kernel can be written as

$$k(t) = \sum_{i=0}^{N_b-1} a'_i \, u(t - iT_b) \quad (5)$$

with

$$a'_i = \begin{cases} 1, & a_i = 1 \\ -1, & a_i = 0 \end{cases} . \quad (6)$$

Since the convolution and correlation are linear operations, their order can be exchanged and Eq. (3) can be rewritten as

$$z(t) = \int_0^\infty h_T(t - \tau) \, z_0(\tau) d\tau \quad (7)$$

with

$$z_0(t) = \left(\frac{2}{N_b+1}\right) \cdot \left(\frac{T_p}{E_t}\right) \cdot \int_0^{T_s} x(\tau) \, k(\tau + t) d\tau \, . \quad (8)$$

Consequently, the cross-correlation function of a RZPN lidar is equal to the convolution of the target impulse response with the normalized cross-correlation function of the transmitted RZPN code with its kernel given in Eq. (8). For a rectangular laser pulse shape, the peak of this cross-correlation function is a triangle with the base equal to two times the laser pulse width. It is a periodic function with the period equal to the PN code length. The target impulse response can be much wider than the laser pulses. It broadens the shape of the peak of the correlation function, but does not cause aliasing.

In practice, the received signal is digitized and so is the kernel. Assuming the signal is digitized at interval $\Delta t_s$, the total number of data points within a PN code period becomes

$$N_s = N_b (T_b / \Delta t_s). \quad (9)$$

As mentioned earlier, the signal is sampled at a fraction of the laser pulse width, i.e., $\Delta t_s \ll T_b$. As a result, the number of data points to process for a RZPN lidar is much larger than that of a conventional PN lidar.

For relatively weak returns, the signal or the correlation results need to be averaged to achieve a sufficient signal-to-noise ratio (SNR). Mathematically, the order of averaging and correlation can be exchanged without affecting the result. In practice the signal is usually averaged first, since signal averaging can be carried out relatively easily and it reduces the data volume to be carried forward.

Finally, a peak search is performed on the outcome of the cross-correlation function. The centroid of the peak gives the target distance, the width of the peak gives an indication of the laser pulse spreading by the target slope and roughness, and the integral of the peak gives the received laser energy, which can be used to infer the surface reflectance.

### *2.4. Comparison to Other Lidar Techniques and Constrainst in RZPN Lidar Applications*

The RZPN lidar technique enables the use of low peak-power lasers for long distance ranging. The efficiency of a PN or RZPN lidar in terms of the average transmitted laser power required to achieve a given receiver SNR is less than a single pulse detection lidar [38], but it enables the use of more efficient lasers, such as fiber lasers. Thus, the overall instrument efficiency can be significantly higher.

A RZPN lidar is far less susceptible than a single pulse lidar to laser speckle noise, which can be a significant noise source for small laser footprint sizes [39,47]. There is still speckle noise in an individual laser pulse return but the they are largely averaged out over many laser pulses within the receiver integration time.

RZPN code modulation permits time division multiplexing of other measurement channels in the return-to-zero time periods. For example, one can insert another measurement channel at a different laser wavelength with a different RZPN code to measure the differential spectral absorption feature of the reflected laser light [37].

The major technical challenge of RZPN lidars is the requirement of more sophisticated signal processing. The receiver has to multiply the received signal with the kernel term by term and sum up all the terms to evaluate a single value of the cross-correlation function. The computation has to be repeated for every time shift of the cross-correlation function within the code length. Because of the narrow laser pulse width and the high signal sampling rate, the total number of computation steps required for a RZPN lidar can be difficult to carry out in real time. However, these computations are all simple and highly repetitive. The computations can be carried in parallel in hardware with available field programmable gate arrays (FPGAs). The correlation function can also be calculated in the frequency domain with the use of Fast Fourier Transform (FFT) and inverse FFT, which reduces the number of computations by many orders of magnitude.

### *2.5. RZPN Lidar for Small Body Missions*

RZPN lidars are suited for small body missions when the ground track speed of the spacecraft is relatively low. RZPN lidars need to integrate the received signal over a relatively long receiver integration time during which the target distance is assumed to be unchanged. In practice, the Doppler shift due to the relative motion between the spacecraft and the target can be pre-compensated by adjusting the sampling clock frequency at the receiver based on the predicted orbit dynamics. However, the surface topography cannot be predicted a priori, which can cause small time shifts in the received RZPN signal sequence and a reduction in the SNR. The residual range rate error in the orbit prediction causes a time expansion or contraction in the received signal which can cause a smear in the averaged signal and, in turn, the cross-correlation function. The smear can be reduced by shortening the signal averaging time and calculating the cross correlation at a high rate, and averaging the correlation functions afterwards. However, this would demand faster signal processing and more resources in the FPGA to carry out the computation. Therefore, RZPN lidars are currently best-suited for a small planetary body mission when the ground track speed is relatively low and target range varies at a relatively slower rate. As the technology of digital signal processing continue to advance, the RZPN lidar technique should be applicable to major planets.

Table 1 lists the rotation parameters and the sizes of the targets of most asteroid and comet missions to date. Based on flown or anticipated spacecraft trajectories in proximity of these bodies, it shows the residual range rate error in the orbit prediction for all small bodies are less than 10 m/s. If we can complete the signal processing from each range measurement within 0.01 s, the total accumulated time error is 0.1 m, or 0.67 ns, which is well within the laser pulse width and should be tolerable. For large bodies like the dwarf planet Ceres, the signal processing would have to be completed much faster.

We have carried out a detailed computer simulation to study the effects of range rate uncertainty, local topography, orbital effects, and the receiver comparator circuit on the correlation results. In addition, we have designed and implemented a real-time, FFT-based correlation breadboard using a Xilinx FPGA and the SALi RZPN code. These results will be reported in a future publication.

**Table 1.** List of orbit dynamics of past asteroids and comet missions. References are indicated for measured values. The other values are derived from shape and trajectory data.

| Parameter | 101955 Bennu | 25143 Itokawa | 162173 Ryugu | 67P/Churyumov-Gerasimenko | 433 Eros | Ceres |
|---|---|---|---|---|---|---|
| Mean Diameter | 492 m [1] | 330 m [1] | 896 m [3] | 3.3 km [5] | 16.8 km [1] | 939.4 km [1] |
| Rotation Period | 4.3 hours [1] | 12.1 hours [1] | 7.6 hours [1] | 12.8 hours [1] | 5.3 hours [1] | 9.1 hours [1] |
| Bond albedo | 4.6% [1] | 27% [2] | 4.0% [4] | 6.2% [6] | 25% [1] | 9.0% [1] |
| Topography | ± 35 m | ± 200m | ± 50 m | ± 2 km | ± 10 km | ± 10 km |
| Reference Mission | OSIRIS-REx | Hayabusa | Hayabusa2 | *CAESAR* [7,8] | NEAR | *TBD* [8] |
| Orbit Altitude | <1 to 7 km | 7 to 20 km | 0.1 to 20 km | 2.5 to 10 km [8] | 20 to 200 km | 30-70 km [8] |
| Ground Speed | 2.5 to 7 cm/s | <2 cm/s | <2 cm/s | 10 to 50 cm/s [8] | 1.5 to 5 m/s | 350 m/s [8] |
| Orbit Prediction | | | | | | |
| Residual Range Uncertainty | 30 m | 75 m | 75 m | 500 m[9] | 800 m[9] | 2 km[9] |
| Residual Range Rate Uncertainty | 10 cm/s | 5 cm/s | 10 cm/s | 5 m/s[9] | 7.5 m/s[9] | 200 m/s[9] |

[1] [40]; [2] [41]; [3] [42] ; [4] [43] ; [5] [44] ; [6] [45]; [7] [46]; [8] Notional (future mission); [9] After gross shape obtained

## 3. SALi Instrument Design and Expected Performance

### *3.1. System Design*

A prototype SALi instrument is currently being developed using the RZPN lidar technique. It combines the designs of an existing CubeSat laser communication system [48-51] and a CubeSat integrated detector cooler assembly (IDCA) [29,52], as depicted in in Figure 2. The instrument parameters are given in Table 2. The size and mass given in Figure 2 are preliminary estimates based on the two existing CubeSat subsystems with an aluminum structure and housing. Detailed instrument design is on-going and will be reported at a later time.

The SALi instrument design is modular. The primary focus of the current instrument development effort is the integration of the HgCdTe APD IDCA and real time RZPN signal processing with the FPGA. Other subsystem designs are relatively mature and they can be improved at a later time. For example, beryllium can be used instead of aluminum for the instrument chassis and support structure to improve the thermal conductance and reduce mass. A more efficient fiber laser assembly can be used to reduce the electrical power. A larger receiver telescope can also be used to extend the maximum ranging capability.

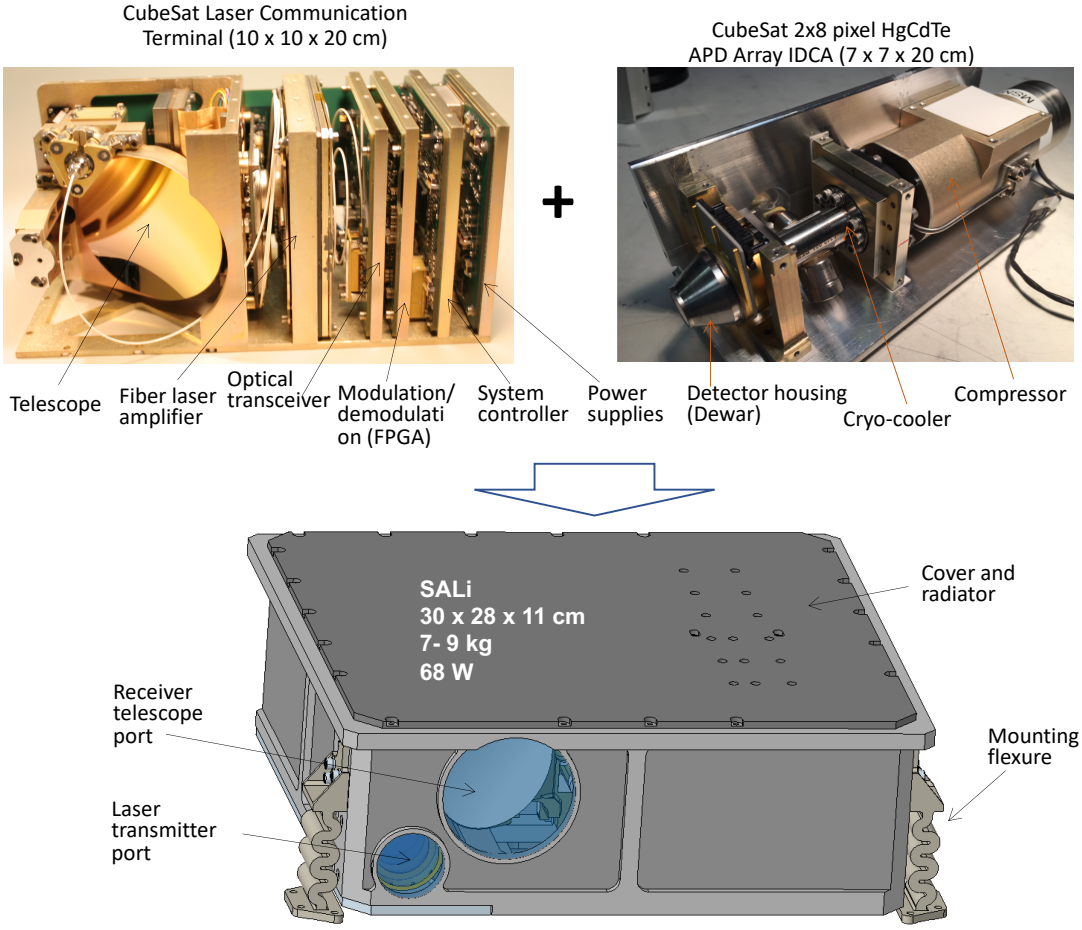


**Figure 2.** Conceptual design of the SALi instrument which combines a CubeSat laser communication terminal [50] with a HgCdTe APD detector-cooler assembly [29,52].

**Table 2.** SALi instrument parameter values.

| Instrument parameters | Values |
|---|---|
| Average laser output power | 2.0 W |
| Laser wavelength | 1.55 µm |
| Beam divergence | 120x480 µrad |
| Transmit optical transmission | 90% |
| Receiver telescope | 6.4 cm diameter |
| Receiver instantaneous field of view (IFOV) | 60x60 µrad |
| Number of pixels | 2x8 |
| Receiver bandwidth | 1.8 nm |
| Optical transmission | 60% |
| Detector quantum efficiency | 50% |
| Detector dark count | 250,000/s |
| Estimated instrument size | 29×28×11 cm |
| Estimated instrument mass | 9.1 kg (aluminum) |
| Estimated power | 68 W |

There are three instrument operation modes: the long-distance survey mode, the mid-altitude mapping mode, and the descent and landing mode. Table 3 lists the instrument parameters for each mode. In the survey mode, all the 16-pixel detector outputs are summed together and the receiver integration time is set to 10 seconds (0.1 Hz) to achieve ranging at >500 km. In this mode, the lidar acts as a single beam lidar to provide a coarse

measurement of the shape and rotation axis of the body. In the mapping mode, all 16 pixels operate independently and provide a 2x8 pixel swath along the ground track. In the landing mode, the instrument is used as a GN&C sensor. The major difference during landing mode operation is that the laser is modulated with periodic pulses (similar to a flash lidar) instead of using the RZPN code. During landing, the instrument provides a real-time multi-pixel target range, spacecraft velocity, and ground surface slope measurements during descent and touchdown.

**Table 3.** SALi operation modes.

| Lidar Parameter | Initial Survey | Mid-Altitude Mapping | Descent and Landing |
|---|---|---|---|
| Mode of operation | Single pixel coarse ranging | 8 to 16 pixels precision ranging | 16-pixel flash lidar |
| Range | 500 to 50 km | 50 to 10 km | 10 km to 1 m |
| *A priori* uncertainty | ± 20 km | ± 200 m | ± 20 m |
| Maximum range rate uncertainty from orbit prediction | < 0.25 m/s | < 0.1 m/s | <0.5 m/s |
| Range rate due to topography | 1 m/s | 1 m/s | - |
| Measurement rate | 0.1 to 1 Hz | 1 to 100 Hz | 10 to 100 Hz |
| Ranging precision and accuracy | 10 m | 0.2 m | 0.05 m |
| Laser footprint diameter | <100 m from 500 km | 6 m at 50 km | N/A |
| Surface reflectance accuracy | ± 20% | ± 5% | N/A |

The parameter values of the RZPN code sequence are given in Table 4. The code was chosen to optimize the lidar performance for the mid-altitude mapping phase of the asteroid investigation. The laser pulse width is 8 ns, which matches the detector impulse response. The signal is sampled at about 1 GHz. The code length is chosen to give a 9.75 km period (range ambiguity) of the correlation function., which coupled with the spacecraft orbit knowledge can be used to determine the absolute target range. The laser illuminates the entire scene subtended by the 2x8 pixel receiver FOV. The signal from each pixel is processed independently but with the same RZPN kernel. The same RZPN code and signal processing algorithm is used for the long-rang (Mode 1) operation but the cross-correlation functions from all 16 receiver channels are summed together, which is equivalent to summing the detected photons from all 16 pixels as one to turn the instrument into a single beam lidar. The results are further averaged over the receiver integration time to achieve the required SNR prior to the peak search. The cross-correlation function is still calculated at 0.1 second interval so that the timing misalignment due to residual uncompensated Doppler shift does not increase due to the longer receiver integration time. If the timing misalignment is still too large, it is possible to lengthen the laser pulse width and the PN code bit time to give a higher tolerance to the timing error.

**Table 4.** RZPN code used in SALi.

| Instrument Parameter | Value |
|---|---|
| PN code length, $N_b$ | 127 bits |
| Bit interval, $T_b$ | 512 ns |
| PN code period, $T_s = T_b N_b$ | 65,024 ns |
| Laser pulse width, $T_p$ | 8 ns |
| Pulse duty cycle, $T_p/(2T_b)$ | 0.78125% |
| Signal sampling interval, $\Delta t_s$ | 1 ns |
| Integration time, $T_I$ | 0.1 to 10 s |

*3.2. Estimated Instrument Performance*

The most important criteria of SALi performance are the probability of target detection, the ranging precision, and the surface reflectance measurement precision. The ranging accuracy depends the frequency stability of the on-board clock and the requirement can be met with a proper choice of the clock oscillator and time keeping between the instrument and the spacecraft.

The target is detected from a peak search of the correlation function. The peak and baseline of the correlation function can be approximated as Gaussian random variable according to the Central Limit Theorem because they are usually a large sum of signal and background photon counts over a relatively long integration time. A matched filter is usually used prior to the peak search to improve the SNR. The peak search is conducted by first finding local peaks above a certain threshold and then compare the local peaks to find the maximum. The threshold is set to a few standard deviations above the mean of the noise floor. The probability of correct detection can be written as

$$P_d = \left[ \int_{-\infty}^{\infty} e^{\frac{-(z_p-\mu_p)^2}{2\sigma_p^2}} \int_{-\infty}^{z_p} e^{\frac{-(z_b-\mu_b)^2}{2\sigma_b^2}} dz_b \, dz_p \right]^{N_{pk}-1} \quad (10)$$

where $\mu_p$ and $\sigma_p^2$ are the mean and variance of the peak of the correlation function, $\mu_b$ and $\sigma_b^2$ are the mean and variance of the baseline of the correlation function, and $N_{pk}$ is the number of local peaks to compare to find the highest one. The local peaks can be from the target return or noise, but the width of the local peaks is limited by the system electrical bandwidth [53], which in this case is limited by the laser pulse width according to Eq. (8). Therefore, we can use $N_{pk} \approx N_b(T_b/T_p)$ when evaluating the probability of target detection.

The mean and variance of the peak of the correlation function with an ideal photon counting detector can be approximated as

$$\mu_p = \langle \dot{n}_s \rangle \, T_I \quad (11)$$

and

$$\sigma_p^2 = \langle \dot{n}_s \rangle \, T_I + (\langle \dot{n}_b \rangle + \langle \dot{n}_d \rangle) \, \frac{T_p}{T_b} \, T_I \quad (12)$$

where $\langle \dot{n}_s \rangle$, $\langle \dot{n}_b \rangle$, and $\langle \dot{n}_d \rangle$ are the average rate of the signal photons, the background photons, and the detector dark noise count, respectively, and $T_I$ is the receiver integration time. It is shown in Eq. (12) that a RZPN lidar reduces the effect of the background photons and the detector dark counts by the ratio of the laser pulse width to the PN bit interval. It is advantages to minimize the laser pulse width while maintaining the same average signal photon rate.

The mean value of the baseline of the correlation function can be assumed to be zero for relatively long PN code. The variance of the baseline when the received laser pulses line up with the kernel in pulse intervals but not the bit pattern is given by

$$\sigma_b^2 = \langle \dot{n}_s \rangle \, T_I + (\langle \dot{n}_b \rangle + \langle \dot{n}_d \rangle) \frac{T_p}{T_b} \, T_I. \quad (13)$$

The variance when the received laser pulses fall within the return-to-zero portion of the kernel becomes

$$\sigma_{b0}^2 = (\langle \dot{n}_b \rangle + \langle \dot{n}_d \rangle) \frac{T_p}{T_b} \, T_I. \quad (14)$$

We can use the worse-case variance given in Eq. (12) for the entire baseline to simplify the calculation.

The ranging precision can be estimated as in conventional lidar [47], as

$$\sigma_R \approx \frac{\sigma_w}{SNR_p} \tag{15}$$

with $\sigma_w$ the root-mean-square (rms) width of the laser pulse width and $SNR_p$ is the SNR of the peak of the correlation function given by

$$SNR_p = \frac{\mu_p}{\sigma_p} = \frac{\langle \dot{n}_s \rangle T_I}{\sqrt{\langle \dot{n}_s \rangle T_I + (\langle \dot{n}_b \rangle + \langle \dot{n}_d \rangle) \frac{T_p}{T_b} T_I}}. \tag{16}$$

The estimated SALi performance based on the above model and with the instrument parameters in Table 2 is shown in Figure 3 for the nominal mapping operation at mid altitude and long-distance survey operation from a much longer distance. For the mapping operation, we assumed all 16 individual pixels operating independently at 0.1 second integration time. For the long-distance reconnaissance operation, we assumed that all the 16 receiver channels are combined and the integration time is increased to 10 seconds. The surface reflectance (albedo) was assumed to be 10% at 1.55 μm wavelength, including the opposition effect [54]. The solar distance was taken as 1 AU for a hypothetical mission to a NEO. Pulse broadening due to surface slope is negligible due to the small instantaneous field of view (IFOV) and relatively wide laser pulse. We also assumed that the Doppler shift in the received signal has been properly compensated and its effects can be neglected.

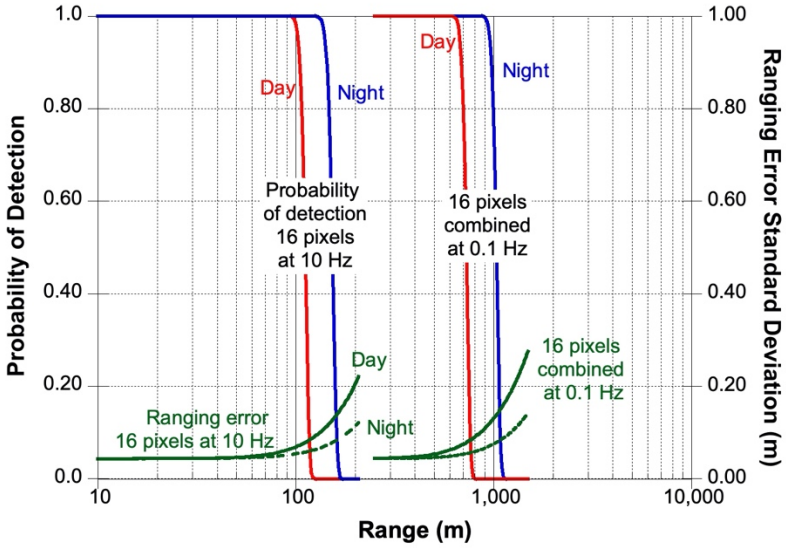


**Figure 3.** Estimated SALi ranging performance based on the above model and instrument parameters given in Table 2.

### *3.3. Laser Transmitter and Optics*

The design of the laser transmitter and the optics are nearly identical to those used in the Compact Laser Communication Terminal (CLCT), a free-space laser communication demonstration [49,51]. The major differences are: (a) SALi uses a separate laser beam collimator (expander) instead of sharing the same telescope with the receiver telescope; (b) SALi does not need the laser pointing mechanism (fast steering mirror) used in CLCT; and (c) SALi uses a HgCdTe APD array detector with a cryo-cooler instead of the InGaAs photodiode in CLCT.

The laser transmitter consists of a seed laser and an erbium dopped fiber amplifier (EDFA) at 1.55 μm wavelength. It was originally designed for transmitting a 64-ary pulse position modulation (PPM) signal at up to 6-W average output power [55]. The laser pulse width, pulse rate, and output power are comparable to those required by SALi. For a small asteroid mission, 2-W average output power is sufficient. As the target distance gets closer, the laser output power can be reduced by at least a factor of 10 by adjusting the pump power of the fiber amplifier. The beam from the fiber laser amplifier is collimated and shaped into a rectangular pattern using a diffractive optical element (DOE) [56] to illuminate the entire scene subtended by the 2x8 pixel HgCdTe APD array. Each pixel has an IFOV of 60x60 μrad. Therefore, the laser beam has a divergence angle of 120x480 μrad. The spatial resolution is the product of the IFOV and spacecraft altitude. A small light deflector is built in at the edge of the laser collimator to scatter a small amount (<1%) laser energy off-axis to allow target range measurement down to <2 m when the transmitted laser beam and the receiver FOV no longer completely overlap due to the bistatic design.

The receiver telescope, shown in Figure 4, is designed to fit in a 1-U CubeSat volume and features an afocal off-axis Cassegrain reflector with an 8x magnification. To provide the largest possible aperture in the available volume the primary mirror has an effective numerical aperture of 1.3. The protected-gold-coated diamond-turned aluminum mirrors are integral to the all-aluminum structure, so no thermal metering is required. The aft optics consists of an optical bandpass filter and a set of focusing lenses to set the 60x60 μrad IFOV. The entire telescope structure is thermally stable and has already been space-qualified [51].

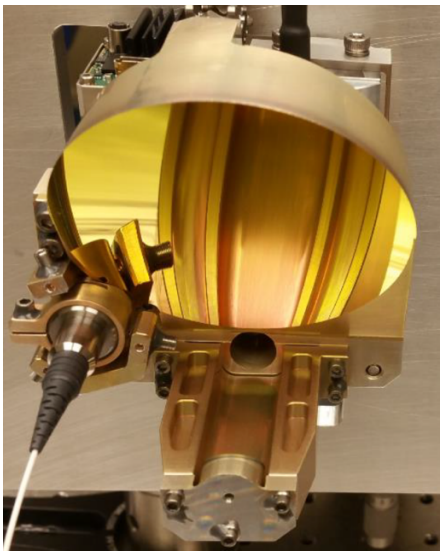

**Figure 4.** Photograph of the receiver telescope from the CubeSat laser communication [49] to be used for SALi. It features an afocal off-axis Cassegrain reflector with a clear aperture of 6.4 cm diameter and 8 times magnification. The optical fiber feed on the lower left of the photograph was for laser communication and will not be needed for SALi.

In the current SALi design, the focus of the telescope and aft optics is fixed to an intermediate distance such that it can give a near optimal performance when mapping of the asteroid or the comet core but still acceptable performance when becoming out of focus at longer target range. During the spacecraft touch-and-go (TAG) maneuver at close up distance, the out of focus can become so severe that the IFOVs subtended by all pixels overlap and SALi becomes a single beam laser range finder. A focusing mechanism can be added in the aft optics assembly if a multipixel measurement is needed.

*3.4. Detector Cooler Assembly*

The SALi detector assembly consists of a 2x8 pixel HgCdTe APD array [57,58] in a miniature Stirling cooler [59]. The HgCdTe APD has a near 90% quantum efficiency over the 0.9 to 4.3-μm spectral range. The APD gain is near deterministic gain and there is little excess noise added when the photoelectrons are multiplied. The APD gain is >1000 such that the photocurrent can completely override the preamplifier electronics noise and single photon event can be detected.

The output of the HgCdTe APD is linear to the incident optical signal power. When there are multiple photons in a received laser pulse, the output becomes the linear sum of pulse waveforms from individual detected photons without any dead-time or other nonlinear effects. The APD has a factor of 100 linear dynamic range at a fixed APD gain. The APD gain can be adjusted by a factor of 1000. Together with the laser power adjustment, SALi can have at least six orders of magnitude dynamic range.

The pixels size of the current devices is 20-μm in diameter on a 64-μm pitch in a 2x8 format. Larger pixel arrays with more pixels are possible in the future. The use of HgCdTe APDs enables the use of other type of laser at wavelengths from near to mid infrared. The HgCdTe APD arrays have been tested for radiation damage and shown to be suitable for use in a typical planetary mission [60].

The HgCdTe APD array operates at 110 K and a cryo-cooler is required. The cooler used in the current IDCA is a military off-the-shelf miniature Stirling cooler [59]. It is designed for operation in sub-orbital and harsh operation environments and has also demonstrated a multi-year operational lifetime.

An IDCA with the same HgCdTe APD array and the cooler has already been developed for a CubeSat demonstration [52]. A microlens array is used on top of the APD array which effectively brings the detector fill factor to near 100%. The IDCA with the microlens array has been laboratory tested per the NASA General Environment Verification Standard (GEVS). A more detailed description of the test results of the HgCdTe APD and the IDCA can be found in [29]. The IDCA for SALi is the same as the previous ones but with the compressor and the cooler rearranged (Figure 5). There is also a major improvement in the cold shield and cold filter design to reduce the stray thermal photons. The cold shield aperture is chosen to give a numerical aperture of 0.14 (f/7). The cold filter has two pass bands, one from 1.00 to 1.13-μm and the other from 1.40 to 1.70-μm, for use with 1.03-μm or 1.55-μm fiber lasers, which are the most common types of fiber lasers from the industry at present. The thermal background photons from the f/7 cold aperture over these two passband are negligible compared to the detector dark noise. The cold filter passband can be fixed after the exact laser wavelength is known. The out-of-band rejection of > 6 optical density (OD). The combination of the cold shield and the cold filters ensures that thermal photons through the cold aperture and stray thermal photons around the cold shield are much lower than the intrinsic dark counts of the detector. The net weight of the IDCA is about 0.80 kg. The total electrical power consumption is about 7 W with the detector chip at 110 K and the IDCA housing at room temperature.

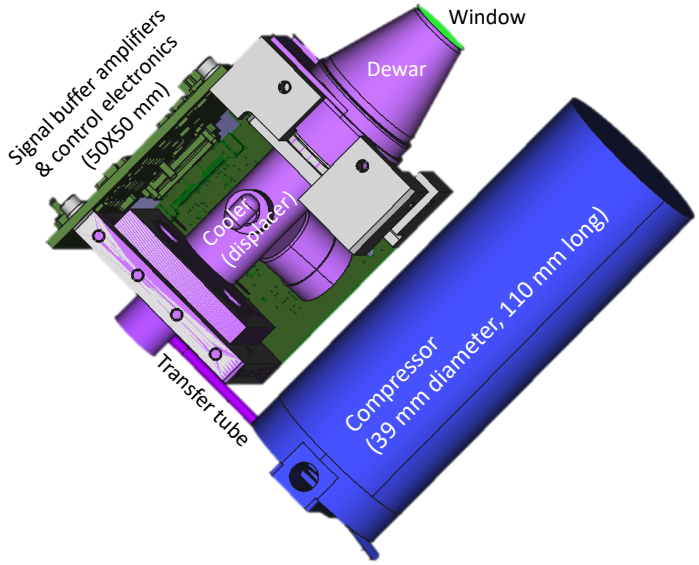


**Figure 5.** A computer-assisted design (CAD) drawing of the integrated detector cooler assembly (IDCA) for SALi.

### *3.5. Electronics*

A major technical challenge for SALi is the receiver electronics that can process multi-channel RZPN signals in real time. Our previous RZPN lidar demonstrations post-processed the signal and kernel in software [36,37], which took minutes to process one measurement for a similar RZPN code and signal sampling rate. For SALi, we have to process 16 channel signals in real time by taking advantages of FPGA and digital signal processing technologies.

Figure 6 shows a function block diagram of SALi. The laser and the associated electronic circuits for the laser transmitter are identical to those used in the laser communication demonstration [48-51]. The signal processing electronics is also the same but with the FPGA reprogrammed for the RZPN lidar signal processing. The system controller for command and data handling (C&DH) and the DC power converters shown in Figure 6 are also the same as those used in the CubeSat laser communication demonstration.

A clock generation circuit is added that generates the clock for the transmitted RZPN code and the receiver signal sampling clock. The clock for the received signal is locked to the transmitter clock but with an offset to compensate for the Doppler shift due to the relative motion between the spacecraft and the target body. The Doppler shift is estimated based on the predicted orbit dynamics. Both clocks are locked to an external reference clock, which is currently a temperature compensated crystal oscillator (TCXO) but can be replaced with a chip scale atomic clock (CSAC) [61], if very precise timing is needed.

The pulse waveforms from each of the 2x8 pixels are digitized before being processed by the FPGA. To reduce the electrical power consumption, a bank of comparators is used as 1-bit digitizers instead of regular 8-bit analog-to-digital converters (ADCs). The threshold levels for the comparators are dynamically adjusted according to the signal level. A single separate ADC is used to digitize the sum of all detector outputs to monitor the received signal level and control the comparator threshold, the laser power, and the detector gain. For weak signals, the detector gain is set to the highest and the thresholds are lowered to just above the noise floor such that the detector is in single photon counting mode. For strong signals, the detector gain is lowered and the thresholds are raised to detect only multi-photon signal pulses and reject most of the background and detector noises. The use of comparators causes quantization errors for strong signals, but the losses in SNR are more than compensated by the stronger signal and lower noise count rate.

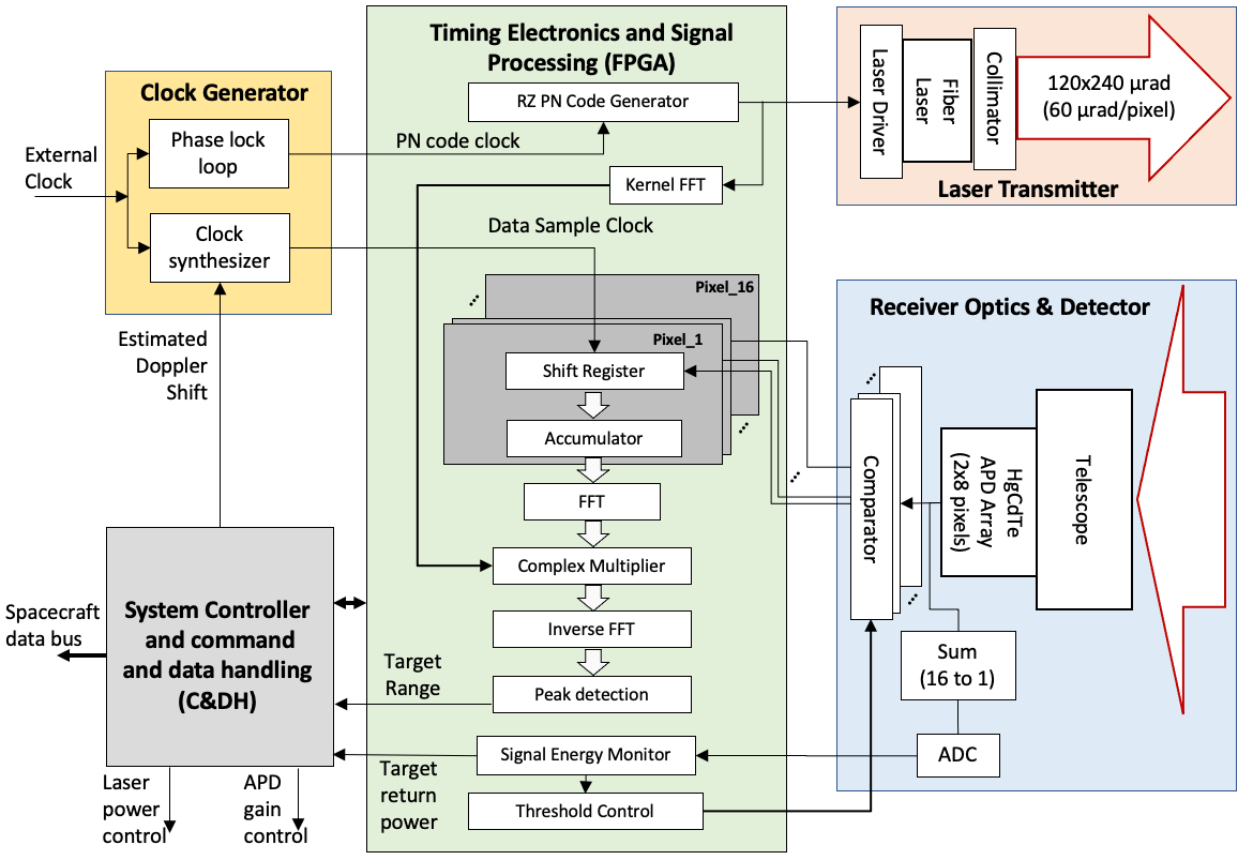


**Figure 6.** Block diagram of SALi instrument and electronics.

### *3.6. FPGA Design*

The FPGA is used to generate the RZPN code to modulate the laser transmitter and process the received signal to locate the target and calculate the laser pulse time of flight and average received laser power.

The PN code is generated using the standard technique with a series of shift registers and logic feedbacks [34]. The pulse width of the PN code signal is reduced to give the specified RZPN pattern. The signal is then amplified to drive the laser.

The received signal from each pixel is serially fed into a shift register bank which periodically shifts out the content to an accumulator (histogrammer), which accumulates the signal over the RZPN code period. The range bin size of the histogrammer is the same as the signal sampling interval and the integration time of the histogrammer is set to 0.1 s, or 1,538 codes. The cross correlation of the accumulated signal with the kernel is carried out in the frequency domain using FFTs, complex multiplication, and IFFTs. A peak search is conducted to locate the target return and determine the ambiguous range, return pulse width and energy. There are 16 sets of signal accumulation circuits, one for each pixel. The cross-correlation is carried out in series using one set of FFT/IFFT circuits. For the long-distance survey operation, the cross-correlation functions from all 16 pixels are summed together and then averaged up to 10 second integration time before the peak search. For short distance measurement during descent and landing, the laser is modulated with periodic pulses at about 65 kHz instead of a RZPN code. The received signals are sampled and histogrammed the same way but skip the FFT/IFFT and go directly to the peak search.

The FPGA also processes the ADC signal and estimates the received signal and noise power and dynamically control the comparator threshold with the use of a standard

control loop. The system controller dynamically adjusts the laser power and the APD gain via a software control loop based on the target return signal power and the background power.

We have implemented the receiver processing algorithm in a breadboard test system using National Instruments (NI) FPGA hardware and LabVIEW software. The RZPN code and kernel were generated and the code transmitted and received in a loopback fashion. The received signal was histogrammed and correlated with the kernel in frequency space using the FFT method described above. A detailed description of that work will be described in a separate publication. We have verified that the correlation operation for each pixel can be carried out in < 1 ms for the RZPN code specified in Table 4 using a Xilinx KU060 FPGA. This allows the system to process the ranges for all 16 pixels in less than 10 ms, which meets the design criterion of a 100 Hz measurement rate.

## 4. Conclusions

A small all-range lidar (SALi) is described, which is specially designed for small planetary body investigations. The lidar uses return-to-zero pseudo-noise (RZPN) code laser modulation and correlation detection, which enables the use of low peak-power but high pulse-rate fiber lasers for long-distance ranging without aliasing. A newly developed, 2x8 pixel linear mode photon-counting HgCdTe avalanche photodiode (APD) array is used which gives a near quantum limited receiver sensitivity from 0.9 to 4 μm wavelengths. The laser power and the APD gain can both be adjusted to give six orders of magnitude dynamic range, enabling measurements from hundreds of kilometers to the surface. A prototype instrument is currently being built by leveraging designs of the laser, optics, and electronics originally developed for a CubeSat free-space laser communication demonstration. The lidar is designed to operate in three modes, including reconnaissance at a long and safe distance, high-resolution mapping from orbit, and real-time multi-spot range and velocity measurements during descent and touchdown. The combination of the fiber lasers, RZPN code modulation, and pixelated infrared single photon detection collectively form a new class of planetary lidars, which is compact, low mass, and ideal for asteroid and comet core missions.

## 5. Patents

The development of the RZPN lidar technique has resulted in a US Patent, 7,982,861 B2, 2011 [29], by Abshire and Sun, who are also authors of this paper.

**Author Contributions:** Conceptualization, X.S., J.A., D.S. and E.M.; methodology, X.S., M.S. and D.C.; electronics design, J.H. and G.Y.; detector, J.B.; cryo-cooler, D.R.; software, J.H. and D.C.; investigation, D.S., M.Z. and E.M.; writing—original draft preparation, X.S. E.M. and D.C.; project administration, X.S., N.M. and N.H.; All authors have read and agreed to the published version of the manuscript.

**Funding:** This research was funded by the NASA GSFC Internal Research And Development (IRAD) programs for Fiscal Years 2008, 2009, 2010, 2013, and 2014. It is currently funded by the NASA Science Mission Directorate (SMD) Maturation of Instrument Technologies for Solar System Exploration (MatISSE) program, Award 18-MatISSE18_0-0029.

**Institutional Review Board Statement:** Not applicable.

**Informed Consent Statement:** Not applicable.

**Data Availability Statement:** Not applicable.

**Acknowledgments:** We thank Mr. Michael Albert, formerly at Fibertek, for the initial optical and system design of the RZPN lidar.

**Conflicts of Interest:** The authors declare no conflict of interest.

## References


1. Sjogren, W. L.; Woffenhaupt, W. R. Lunar shape via the Apollo laser altimeter. *Science* **1973**, *179*, 275–278.
2. Smith, D. E.; Zuber, M. T.; Neumann, G. A.; Lemoine, F. G. Topography of the moon from the Clementine lidar. *J. Geophys. Res.* **1997**, *102*, 1591–1611.
3. Sun, X.; Abshire, J. B.; McGarry, J. F.; Neumann, G. A.; Smith, J. C.; Cavanaugh, J. F.; Harding, D. J., Zwally, H. J.; Smith, D. E.; Zuber, M. T. Space lidar developed at the NASA Goddard Space Flight Center – the first 20 years. *IEEE J. Sel. Top. Appl. Earth Obs. Remote Sens*. **2013**, *6*, 1660-1675.
4. Sun, X. Lidar Sensors from Space. In *Comprehensive Remote Sensing*; Liang, S. Ed.; Elsevier: Oxford, UK, 2018, Volume 1, 412-434.
5. Zuber, M. T.; Smith, D. E.; Cheng, A. F.; Cole, T. D. The NEAR laser ranging investigation. *J. Geophys. Res.* **1997**, *102*, 23761–23773.
6. Cole, T.; Boies, M. T.; El-Dinary, A. S.; Cheng, A.; Zuber, M. T.; Smith, D. E. The NEAR-Earth asteroid rendezvous laser altimeter. *Space Sci. Rev.* **1997**, *82*, 217-253.
7. Tsuno, K.; Okumura, E.; Katsuyama, Y.; Mizuno, T.; Hashimoto, T.; Nakayama, M.; Yuasa, H. Lidar on board asteroid explorer Hayabusa. Proceedings of Sixth International Conference on Space Optics (ICSO), Noordwijk, The Netherlands, 27-30 June 2006, Wilson, A. Ed.
8. Mizuno, T.; Kase, T.; Shiina, T.; Mita, M.; Namiki, N.; Senshu, H.; Yamada, R.; Noda, H.; Kunimori, H.; Nirata, N.; Terui, F.; Mimasu, Y. Development of the laser altimeter (LIDAR) for Hayabusa2. *Space Sci. Rev*. **2016**, *208*, 33-47.
9. Daly, M. G.; Barnouin, O. S.; Dickinson, C.; Seabrook, J.; Johnson, C. L.; Gunningham, G.; Haltigin, T.; Gaudreau, D.; Brunet, C.; Aslam, I.; Taylor, A.; Bierhaus, E. B.; Boynton, W.; Nolan, M.; Lauretta, D. S. The OSIRIS-Rex Laser Altimeter (OLA) investigation and instrument,' *Space Sci Rev.* **2017**, *212*, 899-924.
10. Bus, S. J.; Binzel, R. P. Phase II of the small Main-Belt asteroid spectroscopic Survey: a feature-based taxonomy. *Icarus*, **2002**, *158*, 146-177.
11. DeMeo, F. E.; Binzel, R. P.; Slivan, S. M.; Bus, S. J. An extension of the Bus asteroid taxonomy into the near-infrared. *Icarus*, **2009**, *202*, 160-180.
12. Mainzer, A.; Grav, T.; Bauer, J.; Masiero, J.; McMillan, R. S.; Cutri, R. M.; Walker R.; Wright, E.; Eisenhardt, P.; Tholen, D. J.; Spahr T.; Jedicke, R.; Denneau, L.; DeBaun, E.; Elsbury, D.; Gautier, T.; Gomillion, S.; Hand, E.; Mo, W.; Watkins, J.; Wilkins, A.; Bryngelson, G. L.; Del Pino Molina, A.; Desai, S.; Gomez Camus, M.; Hidalgo, S. L.; Konstantopoulos, I.; Larsen, J. A.; Maleszewski, C.; Malkan, M. A.; Mauduit, J. C.; Mullan, B. L.; Olszewski, E. W.; Pforr, J.; Saro, A.; Scotti, J. V.; Wasserman, L. H. NEOWISE observations of Near-Earth Objectives: preliminary results. *Astrophys. J.* **2011**, *743*, 156.
13. Morbidelli, A.; Levison, H. F.; Tsiganis, K.; Romes, R. Chaotic capture of Jupiter's Trojan asteroids in the early Solar System. *Nature* **2005**, *435*, 462-465.
14. Levison, H. F.; Bottke, W. F., Gounelle, M.; Morbidelli, A.; Nesvorny, D. Contamination of the asteroid belt by primordial trans-Neptunian objects. *Nature* **2020**, *460*, 364-366.
15. Cheng, A. F. Near-Earth Asteroid Rendezvous: mission overview. *J. Geophys. Res.* **1997**, *102*, 23695–23708.
16. Zuber, M. T.; Smith, D. E.; Cheng, A. F.; Garvin, J. B.; Aharonson, O.; Cole, T. D.; Dunn, P.; Guo, Y.; Lemoine, F. G.; Neumann, G. A.; Rowlands, D. D.; Torrence, M. H. The shape of 433 Eros from the NEAR-Shoemaker Laser Rangefinder. *Science* **2000**, *289*, 2097-2101.
17. Fujiwara, A.; Kawaguchi, J.; Yeomans, D. K.; Abe, M.; Mukai, T.; Okada, T.; Saito, J.; Yano, H.; Yoshikawa, M.; Scheeres, D. J.; Barnouin-Jha, O.; Cheng, A. F.; Demura, H.; Gaskell, R. W.; Hirata, N.; Ikeda, H.; Kominato, T.; Miyamoto, H.; Nakamura, A. M.; Nakamura R.; Sasaki, S.; Uesugi, K. The rubble-pile asteroid Itokawa as observed by Hayabusa. *Science* **2006**, *312*, 1330-1334.
18. Thomas, N.; Sierks, H.; Barbieri, C.; Lamy, P. L.; Rodrigo, R.; Rickman, H.; Koschny, D.; Keller, H. W. Agarwal, J.; A'Hearn, M. F.; Angrilli, F.; Auger, A. T.; Barucci, M. A.; Bertaux, J. L.; Bertini, I.; Besse, S.; Bodewits, D.; Cremonese, G.; Deppo, V. D.; Davidsson, B.; De Cecco, M.; Debei, S.; El-Maarry, M. R.; Ferri, F.; Fornasier, S.; Fulle, M.; Giacomini, L.; Groussin, O.; Gutierrez, P. J.; Guttler, C.; Hviid, S. F.; Ip, W. H.; Jorda, L. Knollenberg, J.; Kramm, J. R.; Kuhrt, E.; Kuppers, M.; Forgia, F. L.; Lara, L. M.; Lazzarin, M.; Moreno, J. J. L.; Magrin, S.; Marchi, S.; Marzari, F.; Massironi, M. Michalik, H.; Moissl, R.; Mottola, S.; Naletto, G.; Oklay, N.; Pajola, M.; Pommerol, A.; Preusker, F.; Sabau, L.; Scholten, F.; Snodgrass, C.; Tubiana, C.; Vincent, J. B.; Wenzel, K. P. The morphological diversity of comet 67P/Churyumov-Gerasimenko. *Science* **2015**, *347*, aaa0440.
19. Jorda, L.; Gaskell, R.; Capanna, C.; Hviid, S.; Lamy, P.; Durech, J.; Faury, G.; Groussin, O.; Gutierrez, P.; Jackman, C.; Keihm, S. J.; Keller, H. U.; Knollenberg, J.; Kuhrt, E.; Marchi, S. Mottola, S.; Palmer, E.; Schloerb, F. P.; Sierks, H.; Vincent, J. B.; A'Hearn, M. F.; Barbieri, C.; Rodrigo, R.; Koshny, D.; Rickman, H.; Barucci, M. A.; Bertaux, J. L.; Bertini, I.; Cremonese, G.; Da Deppo, V.; Davidsson, B.; Debei; S.; De Cecco, M.; Fornasier, S.; Fuule, M.; Guttler, C.; Ip, W. H.; Kramm, J. R.; Lara, L. M.; Lazzarin, M.; Lopez Moreno, J. J.; Marzari, F.; Naletto, G.; Oklay, N.; Thomas, N.; Tubiana, C.; Wenzel, K. P. The global shape, density and rotation of Comet 67P/Churyumov-Gerasimenko from preperihelion Rosetta/OSIRIS observations. *Icarus* **2016**, *277*, 257-278.
20. Park, R. S.; Vaughan, A. T.; Konopliv, A. S.; Ermakov, A. I.; Mastrodemos, N.; Castillo-Rogez, J. C.; Joy, S. P.; Nathues, A.; Polanskey, C. P.; Riedel, J. E.; Raymond, C. A.; Russell, C. T.; Zuber, M. T. High-resolution shape model of Ceres from stereophotoclinometry using Dawn imaging data. *Icarus*, **2018**, *319*, 812-827.
21. Morota, T.; Sugita, S.; Cho, Y.; Kanamaru, M.; Tatsumi, E.; Sakatani, N.; Honda, R.; Hirata, N.; Kikuchi, H.; Yamada, M.; Yokota, Y.; Kameda, S.; Matsuoka, M.; Sawada, H.; Honda, C.; Kouyama, T.; Ogawa, K.; Suzuki, H. Yoshioka, K.; Hayakawa, M.; Hirata, N.; Hirabayashi, M.; Miyamota, H.; Michikami, T.; Hiroi, T.; Hemmi, R. Barnouin, O. S., Ernst, C. M.; Kitazato, K.; Nakamura,

T.; Riu, L.; Senshu, H.; Kobayashi, H.; Sasaki, S.; Komatsu, G.; Tanabe, N.; Fujii, Y.; Irie, T.; Suemitsu, M.; Takaki, N.; Sugimoto, C.; Yumoto, K.; Ishida, M.; Kato, H.; Moroi, K.; Domingue, D.; Michel, P.; Pilorget, C.; Iwata, T.; Abe, M.; Ohtake, M.; Nakauchi, Y.; Tsumura, K.; Yabuta, H.; Ishihara, Y.; Noguchi, R.; Matsumoto, K.; Miura, A.; Namiki, N.; Tachibana, S.; Arakawa, M.; Ikeda, H.; Wada, K.; Mizuno, T.; Hirose, C.; Hosoda, S.; Mori, O.; Shimada, T.; Soldini, S.; Tsukizaki, R.; Yano, H.; Ozaki, M.; Takeuchi, H.; Yamamoto, Y.; Okada, T.; Shimaki, Y.; Shirai, K.; Iijima, Y.; Noda, H.; Kicuchi, S.; Yamaguchi, T.; Ogawa, N.; Ono, G.; Mimasu, Y.; Yoshikawa, K.; Takahashi, T.; Takei, Y.; Fujii, A.; Nakazawa, S.; Terui, F.; Tanaka, S.; Yoshikawa, M.; Saiki, T.; Watanabe, S.; Tsuda, Y. Sample collection from asteroid (162173) Ryugu by Hayabusa2: Implications for surface evolution. *Science* **2020**, *368*, 654-659.

22. Lauretta, D. S.; Balram-Knutson, S. S.; Beshore, E.; Boynton, W. V.; Drouet D'Aubigny, C.; DellaGiustina, D. N.; Enos, H. L.; Golish, D. R.; Hergenrother, C. W.; Howell, E. S.; Bennett, C. A.; Morton, E. T.; Nolan, M. C.; Rizk, B.; Roper, H. L.; Bartels, A. E.; Bos, B. J.; Dworkin, J. P.; Highsmith, D. E.; Lorenz, D. A.; Lim, L. F.; Mink, R.; Moreau, M. C.; Nuth, J. A.; Reuter, D. C.; Simon, A. A.; Bierhaus, E. B.; Bryan, H B.; Ballouz, R.; Barnouin, O. S.; Binzel, R. P.; Bottke, W. F.; Hamilton, V. E.; Walsh, K. J.; Chesley, S. R.; Christensen, P. R.; Clark, B. E.; Connolly, H. C.; Crombie, M. K.; Daly, M. G.; Emery, J. P.; McCoy, T. J.; McMahon, J. W.; Scheeres, D. J.; Messenger, S.; Nakamura-Messenger, K.; Righter, K.; Sandford, S. A. RSIRIS-REx: sample return from asteroid (101955). *Space Sci. Rev*. **2017**, *212*, 925-984.
23. Pierrottet, D.; Amzajerdian, F.; Petway, L.; Barnes, B.; Lockard, G.; Hines, G. Navigation Doppler lidar sensor for precision altitude and vector velocity measurements: flight test results. *Proc. SPIE*, **2011**, 8044, 80440S.
24. Xu, W.; Yu, H., Jian, H.; Tong, P. Kuang, Y.; Li, M.; Shu, R. Navigation Doppler lidar sensor for precision landing of China's Chang'E-5 lunar lander. *Appl. Opt.* **2020**, *59*, 8167-8174.
25. Carson III, J. M.; Munk, M. M.; Sostaric, R. R. Estes, J. N.; Amzajerdian, F.; Blair, J. B.; Rutishauser, D. K.; Restrepo, C. I.; Cianciolo, A. D.; Chen, G. T.; Tse, T. The SPLICE project: continuing NASA development of GN&C technologies for safe and precise landing. Proc. AIAA SciTech Forum, San Diego, CA, USA, 7-11 January 2019, Paper AIAA 2019-0660.
26. Jiang, X.; Li, S.; Tao, T. Innovative hazard detection and avoidance guidance for safe lunar landing. *Proc. Inst. Mech. Eng. G* **2016**, *230*, 2086-2103.
27. Sornsin, B.; Schort, B. W.; Bourbeau, T. N.; Dahlin, M. J. Global shutter solid state flash LIDAR for spacecraft navigation and docking applications. *Proc SPIE*, **2019**, *11005*, 110050W.
28. Abshire, J. B.; Sun, X. Time delay and distance measurement. US patent 7,982,861 B2, 2011.
29. Sun, X.; Abshire, J. B.; Krainak, M. A.; Lu, W.; Beck, J. D.; Sullivan III, W. W.; Mitra, P.; Rawlings, D. M.; Fields, R. A.; Hinkley, D. A.; Hirasuna, B. S. HgCdTe avalanche photodiode array detectors with single photon sensitivity and integrated detector cooler assemblies for space applications. *Opt. Eng*. **2019**, *58*, 067103.
30. Takeuchi, N.; Sugimoto, N.; Baba, H.; Sakurai, K. Random modulation cw lidar. *Appl. Opt.* **1983**, *22*, 1382–1386.
31. Takeuchi, N.; Baba, H.; Sakurai, K. Ueno, T. Diode-laser random-modulation cw lidar. *Appl. Opt.* **1986**, *25*, 63–67.
32. Rall, J. A. R. Differential Absorption Lidar Measurements of Atmospheric Water Vapor Using a Pseudonoise Code Modulated AlGaAs Laser, Ph.D. Thesis, The American University, Washington DC, USA, 1993, also in NASA Technical Memorandum 104610, 1994, https://ntrs.nasa.gov/citations/19950005584.
33. Dobler, J. T.; Harrison, F. W.; Browell, E. V.; Lin, B.; McGregor, D.; Kooi, S.; Choi, Y.; Ismail, S. Atmospheric $CO_2$ column measurements with an airborne intensity-modulated continuous wave 1.57 μm fiber laser lidar. *Appl. Opt*. **2013**, *52*, 2874-2892.
34. Dixon, R. C. *Spread Spectrum Systems*, 3rd Ed.; John Wiley & Sons, New York, USA, 1994.
35. Sun, X.; Abshire, J. B.; Krainak, M. A.; Hasselbrack, W. B. Photon counting pseudorandom noise code laser altimeters. *Proc SPIE* **2007**, *6771*, 67710O.
36. Sun, X. and Abshire, J. B. Modified PN code laser modulation technique for laser measurement, *Proc. SPIE* **2009**, *7199*, 71990O.
37. Burris, J. Range resolved $CO_2$ atmospheric backscattering measurements using fiber lasers and RZPN code modulation. American Geophysical Union Fall Meeting, San Francisco, USA, 5 Dec. 2011, Abstract A21D-0096.
38. Machol, J. L. Comparison of the pseudorandom noise code and pulsed direct-detection lidars for atmosphere probing. *Appl. Opt.* **1997**, 36, 6021-6023.
39. Goodman, J. W. Some effects of target-induced scintillation on optical radar performance. *Proc. IEEE* **1965**, *55*, 1688-1700.
40. JPL Small-Body Database Browser. Available online: URL https://ssd.jpl.nasa.gov/sbdb.cgi (accessed on 21 Feb. 2021).
41. Tatsumi, E.; Domingue, D.; Hirata, N.; Kitazato, K.; Vilas, F.; Lederer, S.; Weissman, P. R.; Lowry, S. C.; Sugita, S. Vis-NIR disk-integrated photometry of asteroid 25143 Itokawa around opposition by AMICA/Hayabusa. *Icarus*, **2018**, 311, 175-196.
42. Watanabe, S.; Hirabayashi, M.; Hirata, N.; Hirata, Na.; Noguchi, R.; Shimaki, Y.; Ikeda, H.; Tatsumi, E.; Yoshikawa, M.; Kikuchi, S.; Yabuta, H.; Nakamura, T.; Tachibana, S.; Ishihara, Y.; Morota, T.; Takeuchi, H.; Kouyama, T.; Honda, R.; Kameda, S.; Fuse, T.; Miyamoto, H.; Komatsu, G.; Sugita, S.; Okada, T.; Namiki, N.; Arakawa, M.; Ishiguro, M.; Abe, M.; Gaskell, R.; Palmer, E.; Barnouin, O. S.; Michel, P.; French, A. S.; McMahon, J. W.; Scheeres, D. J.; Abell, P. A.; Yamamoto, Y.; Tanaka, S.; Shirai, K.; Matsuoka, M.; Yamada, M.; Yokota, Y.; Suzuki, H.; Yoshioka, K.; Cho, Y.; Tanaka, S.; Nishikawa, N.; Sugiyama, T.; Kikuchi, H.; Hemmi, R.; Yamaguchi, T.; Ogawa, N.; Ono, G.; Mimasu, Y.; Yochikawa, K.; Takahashi, T.; Takei, Y.; Fujii, A.; Hirose, C.; Iwaa, T.; Hayakawa, M.; Hosoda, S.; Mori, O.; Swada, H.; Shimada, T.; Soldini, S.; Yano, H.; Tsukizaki, R.; Ozaki, M.; Iijima, Y.; Ogawa, K.; Fujimoto, M.; Ho, T.-M.; Moussi, S.; Jaumann, R.; Bibring, J.-P.;Karuse, C.; Ferui, F.; Saiki, T.; Nakazawa, S.; Truda, Y. Hayabusa2 arrives at the carbonaceous asteroid 162173 Ryugu – a spinning top-shaped rubble pile. *Science* **2019**, 364, 268-272.
43. Tatsumi, E.; Domingue, Schröder, S.; Yokota, Y.; Kuroda, D.; Ishiguro, M.; Hasegawa, S.; Hiroi, T.; Honda, R.; Hemmi, R.; Le Corre, L.; Sakatani, N.; Morota, T;. Yamada, M.; Kameda, S.; Koyama, T.; Suzuki, H.; Cho, Y.; Yoshioka, K.; Matsuoka,

M.; Honda, C.; Hayakawa, M.; Hirata, N.; Hirata, N.; Yamamoto, Y.; Vilas, F.; Takato, N.; Yoshikawa, M.; Abe, M.; Sugita, S. Global photometry properties of (162173) Ryugu. *Astronomy & Astrophysics* **2020**, 639, A83.
44. Preusker, F.; Scholten, F.; Matz, K.-D.; Roatsch, T.; Hviid, S. F.; Mottola, S.; Knollenberg, J.; Kührt, E.; Pajola, M.; Oklay, N.; Vincent, J.-B.; Davidsson, B.; A'Hearn, M. F.; Agarwal, J.; Barbieri, C.; Barucci, M. A.; Bertaux, J.-L.; Bertini, I.; Cremonese, G.; Da Deppo, V.; Debei, S.; De Cecco, M.; Fornasier, S.; Fulle, M.; Groussin, O.; Gutiérrez, P. J.; Güttler, C.; Ip, W-H.; Jorda, L.; Keller, H. U.; Koschny, D.; Kramm, J. R.; Küppers, M.; Lamy, P.; Lara, L. M.; Lazzarin, M.; Lopez Moreno, J. J.; Marzari, F.; Massironi, M.; Naletto, G.; Rickman, H.; Rodrigo, R.; Sierks, H.; Thomas, N.; Tubian, C. The global meter-level shape model of comet 67P/Churyumov-Gerasimenko. *Astronomy & Astrophysics* **2017**, 607, L1.
45. Ciarniello, M.; Capaccioni, F.; Filacchione, G.; Raponi, A.; Tosi, F.; De Sanctis, M. C.; Capria, M. T.; Erard, S.; Bockelee-Morvan, D.; Leyrat, C.; Arnold, G.; Barucci, A.; Beck, P.; Bellucci, G.; Fornasier, S.; Longobardo, A.; Mottola, S.; Palomba, E.; Quirico, E.; Schmitt, B. Photometric properties of comet 67P/Churyumov-Gerasimenko from VIRTIS-M onboard Rosetta. *Astronomy & Astrophysics* **2015**, 583, A31.
46. Lauretta, D. S.; Squyres, S. W.; Messenger, S.; Nakamura-Messenger, K.; Nakamura, T.; Glavin, D. P.; Dworkin, J. P.; Nguyen, A.; Clemett, S. Furukawa, Y.; Kimura, Y.; Takigawa, A.; Blake, G.; Zega, T. J.; Mumma M.; Milam. S.; Herd, C. D. K.; and the CAESAR project team. The CAESAR New Prontiers mission: 2. Sample science. 49th Lunar and Planetary Science Conference (LPSC) **2018,** Paper 1334.
47. Gardner, C. S. Target Signatures for Laser Altimeters: an Analysis. *Appl. Opt.* **1982**, *21*, 448-453.
48. Storm, M.; Cao, H.; Litvinovitch, S.; Puffenberger, K.; Young, J.; Pachowicz, D.; Deely, T.; Bupta, S.; Albert, M. Cubesat laser communications transceiver for multi-Gbps downlink. Small Satellite Conference, Logan, UT, USA, 5-10 Aug. 2017, Paper SSC17-XI-09, https://digitalcommons.usu.edu/smallsat/2017/all2017/153/.
49. Storm, M.; Cao, H.; Albert, M.; Engin, D. Cubesat lidar concepts for ranging, topology, sample capture, surface, and atmospheric science. Small Satellite Conference, Logan, UT, USA, 5-10 Aug. 2017, Paper SSC17-S2-03, https://digitalcommons.usu.edu/cgi/viewcontent.cgi?article=3781&context=smallsat.
50. Shelton, M.; Pulkkinen, A.; Summerlin, E. J.; Storm, M. SETH technology demonstration of small satellite deep space optcal communications to aid heliophysics science and space weather forecasting. Small Satellite Conference, Logan, UT, USA, 3-8 Aug. 2019, https://digitalcommons.usu.edu/smallsat/2019/all2019/227/.
51. Mathason, B.; Albert, M. M.; Engin, D.; Cao, H.; Petrillo, K. G.; Hwang, J.; Le, K.; Puffenberger, K.; Litvinovitch, S.; Storm, M.; Utano, R. CubeSat lasercom optical terminals for near-earth to deep space communications. *Proc. SPIE* **2019**, 11910, 1191005.
52. Fields, R.; Sun, X.; Abshire, J.; Beck, J.; Rawlings, R. M.; Sullivan, W.; Hinkley, D. A linear mode photon-counting (LMPC) detector array in a CubeSat to enable science LiDAR measurements. IEEE International Geoscience and Remote Sensing Symposium (IGARSS), Milan, Italy, 26-31 July 2015, pp. 5312-5315, https://ieeexplore.ieee.org/document/7327034.
53. Skolnik, M. L. Introduction to Radar Systems. McGraw-Hill, New York, USA, 1962, 31-32.
54. Hapke, B. *Theory of Reflectance and Emittance Spectroscopy*, Cambridge Univ. Press, New York 2012.
55. Gupta, S.; Engin, D.; Pachowicz, D.; Fouron, J.-L.; Lander, J.; Dang, X.; Litvinowich, S.; Chuang, T.; Puffenberger, K.; Kimpel, F.; Utano, R.; Wright, M. Development, testing, and initial space qualification of 1.5-µm high-power (6W) pulse-position-modulated (PPM) fiber laser transmitter for deep-space laser communication, *Prof. SPIE* **2016**, 9739, 97390V.
56. Smith, J. G., Ramos-Izquierdo, L., Stockham, A.; Scott, S. Diffractive optics for Moon topography mapping. *Proc. SPIE* **2006**, *6223*, 622304.
57. Kinch, M. A. State-of-the-Art Infrared Detector Technology. SPIE Press, Bellingham, WA, USA, 2014.
58. Beck, J. D.; Scritchfield, R.; Mitra, P., Sullivan III, W. W.; Gleckler, . D.; Strittmatter, R.; Martin, R. J. Linear mode photon counting with the noiseless gain HgCdTe e-avalanche photodiode. Opt. Eng. 2014, 53, 081905.
59. foRawlings, D.; Averitt, G. A linear drive cryocooler for ultra-small infrared sensor systems. Proc. SPIE, 2014, 9070, 90702R.
60. Sun, X.; Abshire, J. B.; Lauenstein, J. M.; Babu, S. R.; Beck, J. D.; Sullivan III, W. W.; Hubbs, J. E. Proton radiation effects on HgCdTe avalanche photodiode detectors, IEEE Trans. Nucl. Sci. 2021, 68, 27-35.
61. Cash, P.; Krzewick, W.; Machado, P.; Overstreet, K. R.; Silveira, M.; Stanczyk, M.; Taylor, D.; Zhang, X. Microsemi Chip Scale Atomic Clock (CSAC) technical status, applications, and future plans. IEEE European Frequency and Time Forum (EFTF), Turin, Italy, 10-12 Apr. 2018, 65-71, doi: 10.1109/EFTF.2018.8408999.